3-1-2012

Comparative studies of the spectroscopic properties of nd3+: YAG nanocrystals transparent ceramic and single crystal

M. Pokhrel

N. Ray

G. A. Kumar

D. K. Sardar

Recommended Citation

M. Pokhrel, et. al., (2012) Comparative studies of the spectroscopic properties of nd3+: YAG nanocrystals transparent ceramic and single crystal.Optical Materials Express2:3235. DOI: http://doi.org/10.1364/OME.2.000235

Comparative studies of the spectroscopic properties of Nd^{3+}: YAG nanocrystals, transparent ceramic and single crystal

M. Pokhrel, N. Ray, G. A. Kumar, and D. K. Sardar*

Department of Physics and Astronomy, The University of Texas at San Antonio, San Antonio, Texas 78249, USA
**Dhiraj.Sardar@utsa.edu*

Abstract: Detailed comparative spectroscopic studies of Nd^{3+} doped YAG nanocrystals, transparent ceramic and single crystal have been performed. Although most of the radiative spectral properties of Nd^{3+} are almost in good agreement between the three hosts, the non-radiative losses are significantly high in nanocrystals, which are attributed due to the presence of large amount of hydroxyl groups on the nanocrystals surface which deteriorates the quality of the material for laser applications. In addition, wavelength dependent scattering loss for the Nd^{3+} doped YAG nanocrystals is found significantly high compared to those of Nd^{3+} doped single crystal and ceramic.

OCIS codes: (300.1030) Absorption; (300.2140) Emission; (290.5850) Scattering, particles; (260.2510) Fluorescence; (260.6580) Stark effect; (160.4670) Optical materials; (160.4760) Optical properties.

References and links

1. A. Ikesue, "Polycrystalline Nd:YAG ceramics lasers," Opt. Mater. **19**(1), 183–187 (2002).
2. R. Boulesteix, A. Maître, J. F. Baumard, Y. Rabinovitch, and F. Reynaud, "Light scattering by pores in transparent Nd:YAG ceramics for lasers: correlations between microstructure and optical properties," Opt. Express **18**(14), 14992–15002 (2010).
3. S. K. Durrani, K. Saeed, A. H. Qureshi, M. Ahmad, M. Arif, N. Hussain, and T. Mohammad, "Growth of Nd-doped YAG powder by sol spray process," J. Therm. Anal. Calorim. **104**(2), 645–651 (2011).
4. H. Gong, D.-Y. Tang, H. Huang, and J. Ma, "Agglomeration control of Nd:YAG nanoparticles via freeze drying for transparent Nd:YAG ceramics," J. Am. Ceram. Soc. **92**(4), 812–817 (2009).
5. A. Ikesue, K. Kamata, and K. Yoshida, "Effects of Neodymium Concentration on Optical Characteristics of Polycrystalline Nd:YAG Laser Materials," J. Am. Ceram. Soc. **79**(7), 1921–1926 (1996).
6. A. Ikesue, K. Yoshida, T. Yamamoto, and I. Yamaga, "Optical Scattering Centers in Polycrystalline Nd:YAG Laser," J. Am. Ceram. Soc. **80**(6), 1517–1522 (1997).
7. B. R. Judd, "Optical Absorption Intensities of Rare-Earth Ions," Phys. Rev. **127**(3), 750–761 (1962).
8. J. Li, Y. Pan, F. Qiu, Y. Wu, and J. Guo, "Nanostructured Nd:YAG powders via gel combustion: The influence of citrate-to-nitrate ratio," Ceram. Int. **34**(1), 141–149 (2008).
9. J. Li, Y. Pan, F. Qiu, Y. Wu, W. Liu, and J. Guo, "Synthesis of nanosized Nd:YAG powders via gel combustion," Ceram. Int. **33**(6), 1047–1052 (2007).
10. X.-X. Li, W.-J. Wang, G.-B. Qiu, X.-M. Luo, and S.-J. Su, "Preparation of polycrystalline Nd:YAG nanopowders via gel combustion method," Cailiao Kaifa Yu Yingyong **24**, 33–38 (2009).
11. H. Liu, Y. Sang, H. Qin, Y. Lv, and J. Wang, "Spray freeze drying method for preparation of Nd-doped yttrium aluminum garnet micro-sized and nano-sized powders" (Shandong University, China, 2011), 6 pp.
12. J. Lu, M. Prabhu, J. Song, C. Li, J. Xu, K. Ueda, A. A. Kaminskii, H. Yagi, and T. Yanagitani, "Optical properties and highly efficient laser oscillation of Nd:YAG ceramics," Appl. Phys. B **71**(4), 469–473 (2000).
13. Z. Liu, W. Wen, and C. Pang, "Preparation Nd:YAG powder by co-precipitation method and study on the effect of pH," Taoci (Xianyang, China) **41**, 33–35 (2009).
14. L. Wang, L. Zhang, Y. Fan, J. Luo, P. Zhang, and L. An, "Effect of Nd-doping on the optical properties of yttrium aluminum garnet nanopowders," J. Nanosci. Nanotechnol. **8**(3), 1454–1457 (2008).
15. P. Yuan, Y. Wang, B. Li, H. Xu, and J. Wang, "Preparation and characterization of Nd:YAG nano-particles via microwave homogeneous precipitation method," Zhongguo Fenti Jishu **13**, 8–10, 20 (2007).
16. X. Zhang, D. Liu, H. Liu, J. Wang, H. Qin, and Y. Sang, "Microstructural characteristics of Nd:YAG powders leading to transparent ceramics," J. Rare Earths **29**, 585–591 (2011).

#159671 - $15.00 USD Received 15 Dec 2011; revised 3 Feb 2012; accepted 6 Feb 2012; published 8 Feb 2012

17. A. Ikesue, I. Furusato, and K. Kamata, "Fabrication of Polycrystalline, Transparent YAG Ceramics by a Solid-State Reaction Method," J. Am. Ceram. Soc. **78**(1), 225–228 (1995).
18. M. Sekita, H. Haneda, T. Yanagitani, and S. Shirasaki, "Induced emission cross section of Nd:$Y_3Al_5O_{12}$ ceramics," J. Appl. Phys. **67**(1), 453–458 (1990).
19. M. Sekita, H. Haneda, S. Shirasaki, and T. Yanagitani, "Optical spectra of undoped and rare earth (=Pr, Nd, Eu, and Er) doped transparent ceramic $Y_3Al_5O_{12}$," J. Appl. Phys. **69**(6), 3709–3718 (1991).
20. G. A. Kumar, J. Lu, A. A. Kaminskii, K.-I. Ueda, H. Yagi, T. Yanagitani, and N. V. Unnikrishnan, "Spectroscopic and stimulated emission characteristics of Nd^{3+} in transparent YAG ceramics," IEEE J. Quantum Electron. **40**(6), 747–758 (2004).
21. A. Kozłowska, M. Nakielska, D. Podniesiski, H. Wglarz, A. Wajler, Z. Librant, T. Łukasiewicz, and A. Malg, "Comparison of spectroscopic properties of neodymium-doped aluminium garnet (Nd:YAG) ceramics obtained by reactive sintering of Al_2O_3, Y_2O_3 and Nd_2O_3 and by synthesis of nanocrystalline Nd:YAG powders," Proc. SPIE **7934**, 79341B, 79341B-6 (2011).
22. D. K. Sardar, K. L. Nash, R. M. Yow, and J. B. Gruber, "Absorption intensities and emission cross section of intermanifold transition of Er^{3+} in Er^{3+}:Y_2O_3 nanocrystals," J. Appl. Phys. **101**(11), 113115 (2007).
23. D. K. Sardar, D. M. Dee, K. L. Nash, R. M. Yow, and J. B. Gruber, "Optical absorption intensity analysis and emission cross sections for the intermanifold and the inter-Stark transitions of $Nd^{3+}(4f^3)$ in polycrystalline ceramic Y_2O_3," J. Appl. Phys. **100**(12), 123106 (2006).
24. G. Ofelt, "Intensities of crystal spectra of rare earth ions," J. Chem. Phys. **37**(3), 511–520 (1962).
25. A. A. Kaminskii, *Laser Crystals: Physics and Properties* (Springer-Verlag, 1979).
26. A. A. Kaminskii, *Laser Crystals: Their Physics and Properties* (Springer-Verlag, 1990).
27. R. S. Meltzer, S. P. Feofilov, B. Tissue, and H. B. Yuan, "Dependence of fluorescence lifetimes of Y_2O_3: Eu^{3+} nanoparticles on the surrounding medium," Phys. Rev. B **60**(20), R14012–R14015 (1999).
28. W. F. Krupke, M. D. Shinn, J. E. Marion, J. A. Caird, and S. E. Stokowski, "Spectroscopic, optical, and thermomechanical properties of neodymium- and chromium-doped gadolinium scandium gallium garnet," J. Opt. Soc. Am. B **3**(1), 102–114 (1986).
29. D. Chen, Y. Wang, E. Ma, Y. Yu, F. Liu, and R. Li, "Spectroscopic and stimulated emission characteristics of Nd^{3+} in transparent glass ceramic embedding β-YF_3 nanocrystals," J. Appl. Phys. **102**(2), 023504 (2007).
30. D. K. Sardar, R. M. Yow, J. B. Gruber, T. H. Allik, and B. Zandi, "Stark components of lower-lying manifolds and emission cross-sections of intermanifold and inter-Stark transitions of $Nd^{3+}(4f^3)$ in polycrystalline ceramic garnet $Y_3Al_5O_{12}$," J. Lumin. **116**(1-2), 145–150 (2006).
31. A. Kaminskii, K. Ueda, A. Konstantinova, H. Yagi, T. Yanagitani, A. Butashin, V. Orekhova, J. Lu, K. Takaichi, T. Uematsu, M. Musha, and A. Shirokava, "Refractive indices of laser nanocrystalline ceramics based on $Y_3Al_5O_{12}$," Crystallogr. Rep. **48**(5), 868–871 (2003).
32. G. D. Yoder, P. K. Diwakar, and D. W. Hahn, "Assessment of soot particle vaporization effects during laser-induced incandescence with time-resolved light scattering," Appl. Opt. **44**(20), 4211–4219 (2005).
33. W. Chen, *Doped Nanomaterials and Nanodevices* (American Scientific Publishers, 2010).
34. D. Dexter, "A Theory of Sensitized Luminescence in Solids," J. Chem. Phys. **21**(5), 836–850 (1953).
35. B. Di Bartolo and G. Armagan, A. International School of Atomic and Molecular Spectroscopy, *Spectroscopy of Solid-State Laser-Type Materials* (Plenum Press, 1987).
36. D. E. Day and J. M. Stevels, "Effect of dissolved water on the internal friction of glass," J. Non-Cryst. Solids **14**(1), 165–177 (1974).

1. Introduction

With the advancement of nanoscience and nanotechnology, transparent ceramic materials have gained much attention among researchers and photonics industry due to their several potential applications. In the fabrication of the transparent ceramics, the primary step is to synthesize the nanoparticle with proper size and shape so that the grains in the final high pressure sintered compact structure are well distributed with less pores, boundaries and other kinds of defects [1–8]. Optical transparency in polycrystalline materials is limited by the amount of light, which is scattered by their micro structural features [2,6]. The amount of light scattering therefore depends on the wavelength of the incident light. Most ceramic materials, such as Nd^{3+}: YAG, are formed from fine powders, yielding a fine grained polycrystalline microstructure, which is filled with scattering centers comparable to the wavelength of visible light [6,9–12]. Recently different groups have reported the synthesis method to get the uniform shape nanocrystals with a desired microstructure [6,9–16]. Most of this work is concentrated towards the improvement in the microstructure of the nanocrystals, which ultimately improve the ceramic quality by reducing the scattering centers (pores and grains) on the surface of the ceramic [6,17–19]. With the improved methods and technology,

#159671 - $15.00 USD Received 15 Dec 2011; revised 3 Feb 2012; accepted 6 Feb 2012; published 8 Feb 2012

optical quality of ceramics has been greatly enhanced, which has made the ceramic as a highly efficient laser media as reported in several previous publications [18,20,21].

Though the optical, mechanical and thermal properties of the bulk transparent ceramics are important in the final device fabrication, it is also important to understand these properties in the nano or micro structural grains and see how it can change while transforming from smaller size to a bulk transparent structure, especially in doped ceramic structures. Since the optical properties such as absorption, emission, optical gain, etc., can be influenced by the size, shape and distribution of the grains in the final structure. In this work, we are exploring a comparison of various optical properties of Nd doped YAG nanoparticles to those of transparent ceramic and single crystals. A detailed calculation of the inter-Stark emission cross section for the observed emission bands were done and compared with single crystal and transparent ceramic. Further, wavelength dependent scattering loss spectrum for nanocrystals has been calculated and compared with those of ceramics and single crystals. To the best of our knowledge, we are reporting for the first time the detailed comparative analyses of spectroscopic properties of Nd^{3+}: YAG nanocrystals and its counterparts ceramic and single crystals.

2. Experimental detail

2.1 Synthesis and characterization

Nd^{3+} doped YAG nanocrystals were prepared by a precipitation of select rare-earth salts in a urea solution following the procedure outlined in flow chart as shown in Fig. 1 [22]. All chemicals are 99. 9% pure and were purchased from Sigma–Aldrich. $NdCl_3$ (0.128 mM), YCl_3 (2.36 mM), and $AlCl_3$ (3.93 mM) were dissolved on 1.0 M concentrated urea solution set with circulating bath at 90°C for 3 hrs upon constant stir. The OH^- ions were generated through solubility of urea in water.

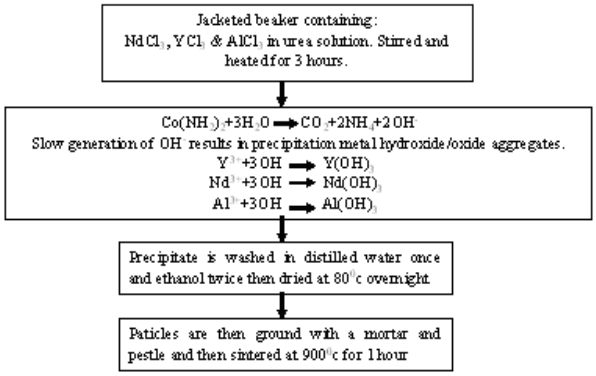

Fig. 1. An overview of synthesis protocol using urea precipitation method.

The result was the formation of rare earth hydroxides. The hydroxides were then filtered from the solution and washed thoroughly with distilled water, ethanol and then dried at 80°C. The dried powder was then finally sintered at 900°C for 1 h to obtain the corresponding Nd: YAG nanoparticles.

The microstructure of the Nd^{3+}: YAG nanocrystal was characterized by scanning transmission electron microscope (STEM). Energy dispersive X-ray (EDX) analyses were carried out using a Hitachi S-5500 at an accelerating voltage of 30 kV. High resolution TEM

#159671 - $15.00 USD Received 15 Dec 2011; revised 3 Feb 2012; accepted 6 Feb 2012; published 8 Feb 2012

analyses were performed using a JEOL JEM-2010F TEM equipped with a field emission gun operated at 200 kV. The digital micrograph software GATAN was used to analyze the TEM images. The sample for XRD measurement was prepared by drying powders and dispersed on a glass substrate. The crystal structure of the sample has been analyzed using X-ray powder diffraction (XRD) at 40 KV and 30 mA in the parallel beam configuration using RIGAKU Ultima IV X-ray diffractometer with Cu Kα (λ = 1.5 A).

The sample for taking the absorption spectra has been prepared by mixing nanocrystals with transparent epoxy in the ratio of two to one and quenched in between two thin transparent glass slab putting epoxy as a reference. Since the nanocrystals were mixed with epoxy, effective index of refraction n_{eff} was used for the calculation. The absorption and transmission spectra were collected for 300–900 nm range using a UV-VIS-NIR spectrophotometer (Cary, Model 14R) in the transmission mode. The near-infrared (NIR) emission spectra were recorded under the excitation at 808 nm band of Ti-Sapphire laser (Spectra Physics, Model 3900S) pumped by an Nd: YAG laser (Spectra Physics, Model Millennia). The emission from the sample was collected with a 1.25 m single grating scanning monochromator (SPEX, Model 1250M) and detected by a liquid nitrogen cooled InGaAs detector (DSS-1GA020L, Electrooptic System Inc) for the NIR and photo multiplier tube at –950V bias (Model 1911, Horiba) for the visible. The fluorescence spectrum for NIR transitions was scanned using a 600 grooves/mm diffraction grating blazed at 1.5 µm, with a spectral resolution of 0.01 nm. The detector signal was processed in a computer coupled to the data acquisition system through a lock in amplifier (Stanford Research System, Model SR510,). The entire system was controlled though the data acquisition software Synerjy (Origin Lab), and HORIBA Jobin-Yvon). For emission lifetime studies, the 808 nm output of a pulsed (5 ns) Nd: YAG pumped MOPO SL optical parametric oscillator (Spectra-Physics, Mountain View, CA) was employed on the dry powder as the pumped source. The decay transients were averaged and recorded using a TDS 220 digital oscilloscope (Tektronix, Beaverton, OR). All measurements were carried out at room temperature. The FTIR vibrational spectrum was measured on the solid sample in the transmission mode using the FTIR spectrometer (Bruker, Model vector 22).

2.2 Phase and morphology

Figure 2(a) shows the X-ray powder diffraction patterns of Nd: YAG powders at 900 °C compared with standard JCPDS data of YAG (01-073-3184). It is clear that the patterns were basically consistent with YAG phase and no additional phases were observed. XRD results reveal that the polycrystalline YAG powder sample has a cubic phase structure with unit cell parameters calculated from the XRD patterns to be a = b = c = 12.061 Å. The values are greater than for pure YAG as expected due to partial substitution of Y^{3+} by Nd^{3+}(it should be a = 12.01 A°, JCPDS No 01-073-3184). From powder X-ray diffraction patterns, the effective crystallite size (particle size) was calculated based on line broadening of XRD peaks. The nanocrystal is constituted by very fine roughly spherical nanoparticles with an average size about ~40 nm, showing a certain tendency to agglomeration.

#159671 - $15.00 USD Received 15 Dec 2011; revised 3 Feb 2012; accepted 6 Feb 2012; published 8 Feb 2012

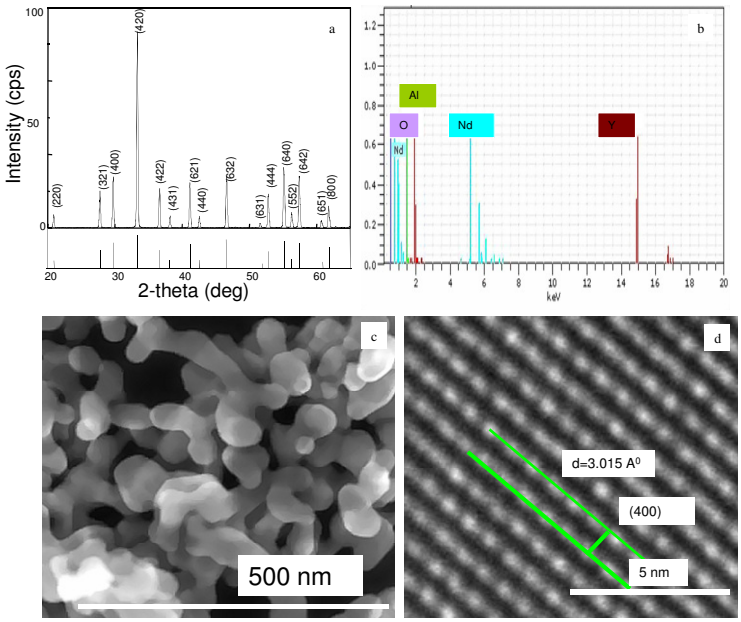

Fig. 2. (a) XRD patterns of Nd^{3+}: YAG nanocrystals and its comparison with the standard patterns of YAG (JCPDS No. 33–0040 (b) EDX spectrum of Nd^{3+}: YAG nanocrystals (c) SEM image of Nd^{3+}: YAG nanocrystals (d) TEM images of (400) plane with lattice spacing.

The samples were analyzed for composition using EDX technique. Figure 2(b) shows the representative EDX pattern for Nd: YAG powder annealed at 900 °C. The presence of Nd peak suggests the doping of Nd into the host. The doping of Nd^{3+} is also confirmed by the absorption spectra as shown in Fig. 3. The quantitative doping concentration analysis on the final product was done based on EDX. The EDX analysis on different clusters shows that the Nd^{3+} concentration on the final product is 1.2 wt %, which is 0.8 wt % less than the initial $NdCl_2$ precursor chosen in the starting composition. The dopant concentration was chosen based on the interest of the single crystal (1wt %) and the ceramic (1wt %) available to us. The morphology and the sizes of the prepared YAG nanocrystals were investigated using scanning electronic microscopy (SEM). Figure 2(c) shows the SEM micrograph taken for the samples annealed at 900°C. The high resolution lattice image for the plane (400) is shown in Fig. 2(d). It can be seen that the Nd: YAG powder is well-crystallized, which supports the XRD. The digital micrograph software was used to estimate the lattice spacing'd' between adjacent lattice planes in the [400] direction as shown in Fig. 2(d).

3. Results and data analysis

3.1. Judd-Ofelt (J-O) calculation

The room temperature UV-VIS-NIR absorption spectra of the sample are shown in Fig. 3 with their spectral band assignments. In calculating the absorption coefficient, the scattering losses were subtracted in all absorption measurements. The inset of the Fig. 4 show the images of the sample, which were analyzed for all the comparative study. It was found that all absorption bands of Nd^{3+} in YAG nanocrystals is similar to those of previously reported for

#159671 - $15.00 USD Received 15 Dec 2011; revised 3 Feb 2012; accepted 6 Feb 2012; published 8 Feb 2012

single crystal and ceramic garnet hosts [12,23]. The spectrum is well resolved so that almost every Stark components corresponding to different manifold of Nd^{3+} are observed.

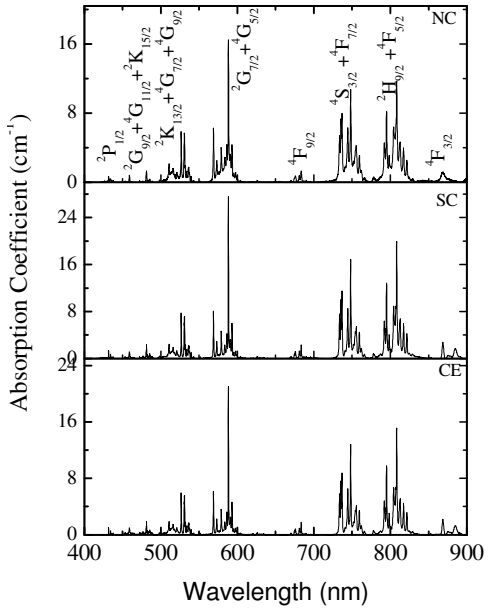

Fig. 3. Absorption spectrum of Nd^{3+}: YAG nanocrystals at room temperature ranging between 300 and 1000 nm compared to ceramics, and single crystals. SC: Single Crystal, CE: Ceramic, and NC: Nanocrystals.

Sixteen absorption bands identified in the room temperature absorption spectra between 300 and 1000 nm, shown in Fig. 3 and are tabulated in Table 1. These absorption bands were chosen to determine the phenomenological Judd-Ofelt parameters [7,17,24] for polycrystalline Nd^{3+}: YAG powder. The effective refractive index n_{eff} was calculated using the following equation as $n_{eff} = xn_{nc} + (1\text{-}x)n_{med}$. Where n_{nc} and n_{med} corresponds to the refractive index of nanocrystals and the medium respectively. The "filling factor" x describes the volume fraction occupied by the nanoparticles aggregates in the surrounding medium, which was estimated to be 0.59. The calculated wavelength dependent effective refractive indexes were reported in Tables 1 and 2. The measured and calculated line strengths are given in Table 1 provided an RMS deviation of 0.20 x 10^{-20} cm^2. The RMS line strength is determined to be 2.70 x 10^{-20} cm^2. The ratio of these two values yields an RMS error of about 7.0%, which is the relative error of fit and falls at the lower end of the range of 5 to 25%, as obtained by the application of the J-O theory to other laser materials [7,24–26]. The J-O parameters for Nd: YAG nanocrystals was calculated to be, $\Omega_2 = 0.22 \times 10^{-20}$ cm^2, $\Omega_4 = 3.15 \times 10^{-20}$ cm^2, and $\Omega_6 = 5.71 \times 10^{-20}$ cm^2, with an RMS error of 7.0% and these values are found to be similar with single crystal and ceramic with some experimental similarities.

These phenomenological J-O parameters were subsequently utilized to determine the emission line strengths corresponding to the transitions from the upper multiplet manifolds $^{2S+1}L_J$ to the corresponding lower lying multiplet manifolds $^{2S'+1}L_{J'}$ of Nd^{3+} in YAG nanocrystals [7,24,25], radiative decay rates from J to J', fluorescence lifetime, and branching ratios for the manifold transitions from $^4F_{3/2}$ to $^4I_{9/2}$, $4I11_{/2}$, $^4I_{13/2}$, and $^4I_{15/2}$, as reported in Table 2. More importantly, the radiative lifetimes are calculated with and without epoxy in the sample. The radiative lifetime without epoxy was calculated to be 244 μs which is shorter (275 μs) by approximately 13% when epoxy was added to the sample. The calculated

#159671 - $15.00 USD Received 15 Dec 2011; revised 3 Feb 2012; accepted 6 Feb 2012; published 8 Feb 2012

radiative lifetime of nanocrystals with epoxy was found to be greater than that of both the single crystal and ceramic. The radiative lifetime of the sample with epoxy is expected to be longer due to the high refractive index of epoxy (1.556) as s surrounding medium compared to refractive index of air (1.0). The result agrees with what was reported by Meltzer and et al [27].

Table 1. Measured and Calculated Absorption Line Strengths of Nd^{3+} in Nd^{3+} Doped YAG Nanocrystal

Transitions from $^4I_{9/2}$	λ (mean)	n_{eff}	Smeas (10^{-20} cm^2)	Scal (10^{-20} cm^2)	$(\Delta S)^2$ (10^{-40} cm^4)
$^2P_{1/2} + {}^2P_{3/2}$	392	1.737	0.193	0.128	0.0042
$^2K_{15/2} + {}^2G_{9/2} + {}^4G_{11/2}$	481	1.727	0.317	0.224	0.0084
$^2K_{13/2} + {}^4G_{7/2} + {}^4G_{9/2}$	531	1.724	0.896	1.00	0.0115
$^2G_{7/2} + {}^4G_{5/2}$	588	1.721	2.473	2.47	0.000
$^4F_{9/2}$	684	1.717	0.314	0.267	0.002
$^4F_{7/2} + {}^4S_{3/2}$	748	1.715	3.705	3.912	0.042
$^4F_{5/2} + {}^2H_{9/2}$	808	1.714	4.00	3.704	0.090
$^4F_{3/2}$	882	1.707	0.799	1.036	0.056
$\Omega_2 = 0.22 \times 10^{-20}$ cm^2, $\Omega_4 = 3.15 \times 10^{-20}$ cm^2, $\Omega_6 = 5.71 \times 10^{-20}$ cm^2, rms deviation = 0.20×10^{-20} cm^2					

Table 2. Predicted Fluorescence line Strengths (S_{calc}), Radiative Decay Rates($A_{jj'}$), Branching Rations ($\beta_{jj'}$), and Radiative lifetime of Nd^{3+}in Nd^{3+} Doped YAG Nanocrystal at 300 K

Transitions	λ (mean)	n_{eff}	S_{calc} (10^{-20} cm^2)	$A_{jj'}$(ED) (s^{-1})	$\beta_{JJ'}$(%)	τ_{rad} (μs)
$^4F_{3/2} \rightarrow {}^4I_{15/2}$	1852	1.700	0.165	21.23	0.6	
$^4I_{13/2}$	1333	1.707	1.191	417.45	11.5	
$^4I_{11/2}$	1053	1.707	2.703	1924.96	52.9	
$^4I_{9/2}$	881	1.713	1.036	1273.21	35.0	275

#159671 - $15.00 USD Received 15 Dec 2011; revised 3 Feb 2012; accepted 6 Feb 2012; published 8 Feb 2012

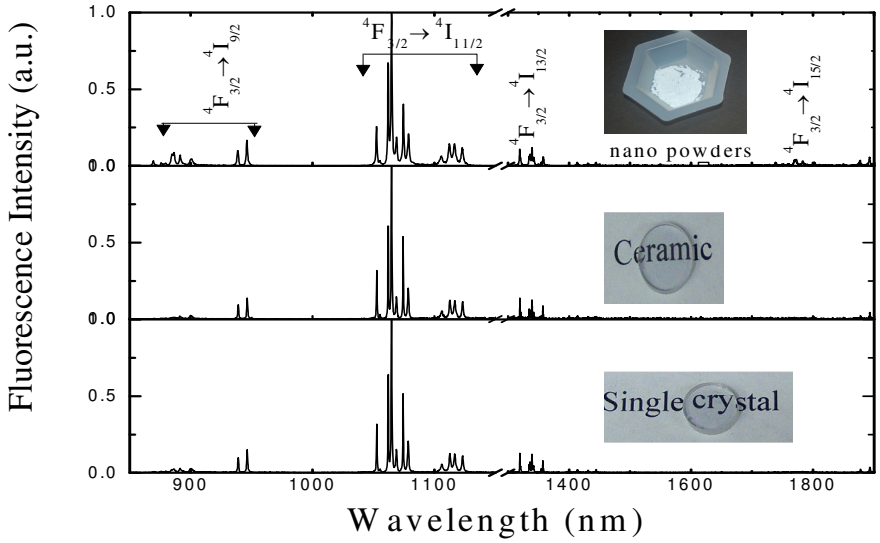

Fig. 4. Fluorescence spectra of Nd^{3+}: YAG nanocrystals within the manifold $^4F_{3/2} \rightarrow {}^4I_{9/2,\ 11/2,\ 13/2,\ 15/2}$ transitions at room temperature compared with ceramic and single crystal. Inset of the figure shows the samples studied for comparison.

3.2 Inter-Stark and intermanifold emission cross sections

The peak emission cross section for the inter-Stark transition is one of the most important parameters of laser design because it describes the maximum spatial amplification of emission intensity. The inter-Stark transition in Nd: YAG nanocrystals are accurately fitted by a Gaussian line shape with a respective full width at half maximum (FWHM). A Gaussian line shape is indicative of inhomogeneous broadening. This inhomogeneity is coming from changes in the local Nd^{3+} site symmetry, due to the substitution from Nd^{3+} ions on the Y^{3+} ion site. All the NIR emission spectra collected for nanocrystals, single crystal and ceramics under 808 nm excitation are shown in Fig. 4. The detailed characterization of the Stark energy levels of the $^4I_{9/2}$, $^4I_{11/2}$, $^4I_{13/2}$, and $^4I_{15/2}$ multiplets have been determined from the room temperature emission spectra within the manifold $^4F_{3/2} \rightarrow {}^4I_{9/2}$, $^4F_{3/2} \rightarrow {}^4I_{11/2}$, $^4F_{3/2} \rightarrow {}^4I_{13/2}$, and $^4F_{3/2} \rightarrow {}^4I_{15/2}$ transitions of Nd^{3+} ($4f^3$) in YAG nanocrystals as shown in Fig. 5 respectively. The energy-level diagrams of the Stark components for the intermanifold $^4F_{3/2} \rightarrow {}^4I_{9/2}$, $^4F_{3/2} \rightarrow {}^4I_{11/2}$, $^4F_{3/2} \rightarrow {}^4I_{13/2}$, and $^4F_{3/2} \rightarrow {}^4I_{15/2}$ transitions are presented in Fig. 6 respectively.

The inter-Stark emission cross sections for all the Stark transitions are determined from the corresponding spectral line shapes provided they are properly resolved as shown in Fig. 5. The peak emission cross sections (σ_p) for all the transitions can be expressed accordingly in the following generalized equations [28–30].

$$\sigma_p\left(R_{1,2} \rightarrow W,X,Y,Z\right) = \frac{\lambda_p^{\ 2}}{4\pi n^2 c \Delta\tilde{\nu}}\left[\frac{\ln 2}{\pi}\right]^{1/2} A\left(R_{1,2} \rightarrow W,X,Y,Z\right), \qquad (1)$$

But for the particular inter-Stark transition such as ($R_1 \rightarrow Y_2$), the following equation is used:

$$\sigma_p\left(R_1 \rightarrow Y_2\right) = \frac{\lambda_p^{\ 2}}{4\pi n^2 c \Delta\tilde{\nu}}\left[\frac{\ln 2}{\pi}\right]^{1/2} A\left(R_1 \rightarrow Y_2\right), \qquad (2)$$

#159671 - $15.00 USD Received 15 Dec 2011; revised 3 Feb 2012; accepted 6 Feb 2012; published 8 Feb 2012

where λ_p is the wavelength at the peak position of the emission band, c is the speed of light, and $\Delta\tilde{\nu}$ is the FWHM line width. The radiative probabilities of the inter-Stark transitions $R_1 \rightarrow Y_2$ can be expressed in the following respective equation [28–30]:

$$A(R_1 \rightarrow Y_2) = \left(1 + e^{-\Delta/kT}\right)\beta(R_1 \rightarrow Y_2) \times \beta\left({}^4F_{3/2} \rightarrow {}^4I_{11/2}\right)\tau\left({}^4F_{3/2}\right)^{-1}, \qquad (3)$$

where Δ is the difference in energy between the Stark levels R_1 and R_2 of the ${}^4F_{3/2}$ manifold. The analyses of absorption and emission spectra corresponding to ${}^4F_{3/2}$ indicate that the ${}^4F_{3/2}$ manifold of Nd^{3+}: YAG polycrystalline powder is split into the Stark components R_1 and R_2 with an energy difference of 92 cm^{-1} ± 0.1 cm^{-1}. Similarly, k is the Boltzmann constant, T is the absolute temperature, τ (${}^4F_{3/2}$) is the radiative lifetime of the ${}^4F_{3/2}$ level, β ($R_1 \rightarrow Y_2$) represent the branching ratios for the corresponding inter-Stark transitions and β (${}^4F_{3/2} \rightarrow {}^4I_{11/2}$) is the branching ratios for the respective intermanifold transitions. The branching ratio for the inter-Stark transition is determined by dividing the area of the sharp inter-Stark transition band to the total area of the intermanifold transition. The constants c and k have their usual meanings and values.

The peak emission cross sections of the inter-Stark transitions obtained for ${}^4F_{3/2} \rightarrow {}^4I_{9/2}$, ${}^4F_{3/2} \rightarrow {}^4I_{11/2}$, ${}^4F_{3/2} \rightarrow {}^4I_{13/2}$, and ${}^4F_{3/2} \rightarrow {}^4I_{15/2}$ are presented in Table 3, Table 4, Table 5, and Table 6 respectively including comparison with single crystal and ceramic. In this comparison study, we found that the inter-Stark cross section for Nd^{3+}: YAG nanocrystal for the inter-Stark transition within the manifold ${}^4F_{3/2} \rightarrow {}^4I_{11/2}$ corresponding to 1064 nm is 4.27 x 10^{-20} cm^2, where inter-Stark cross section for the same transition in single crystal and ceramic are found to be 3.85 x 10^{-20} cm^2 and 3.76 x 10^{-20} cm^2 respectively. This shows that these values are very much similar with single crystals and ceramics with some experimental uncertainties as reported in Tables 3, 4, 5, 6, and 7.

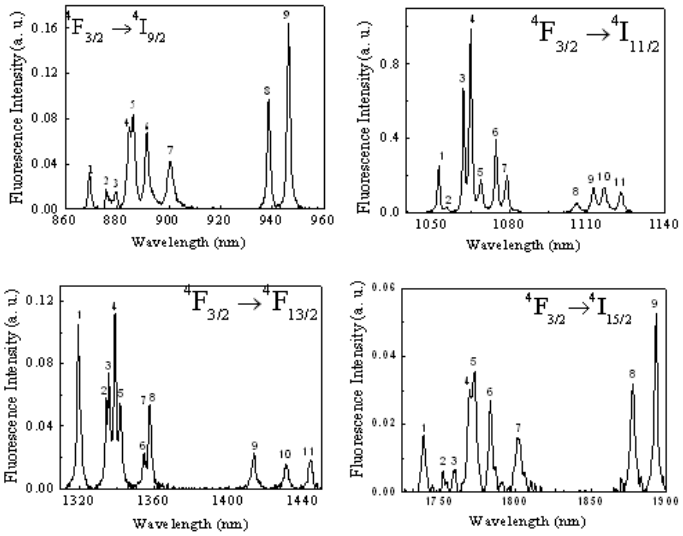

Fig. 5. Fluorescence spectra for Nd^{3+}: YAG nanocrystals within the manifold ${}^4F_{3/2} \rightarrow {}^4I_{9/2}$, ${}^4F_{3/2} \rightarrow {}^4I_{11/2}$, ${}^4F_{3/2} \rightarrow {}^4I_{13/2}$, and ${}^4F_{3/2} \rightarrow {}^4I_{15/2}$ transitions at room temperature.

#159671 - $15.00 USD Received 15 Dec 2011; revised 3 Feb 2012; accepted 6 Feb 2012; published 8 Feb 2012

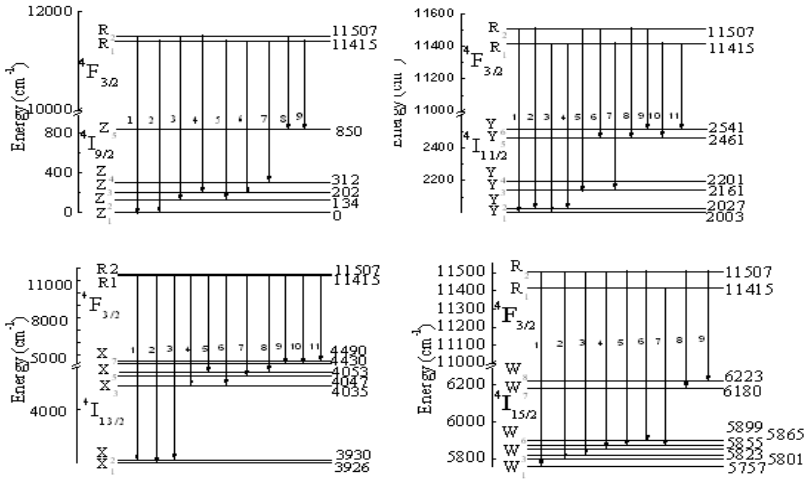

Fig. 6. Energy level diagrams of Nd^{3+}: YAG nanocrystals for the observed inter-Stark transitions within the $^4F_{3/2} \rightarrow {}^4I_{9/2}$ $^4F_{3/2} \rightarrow {}^4I_{11/2}$, $^4F_{3/2} \rightarrow {}^4I_{13/2}$, and $^4F_{3/2} \rightarrow {}^4I_{15/2}$ manifolds transitions at room temperature.

Table 3. Radiative Properties of Various Stark Levels Observed for the Transition within the Manifold $^4F_{3/2} \rightarrow {}^4I_{9/2}$, and Its Comparison with the Single Crystal and Ceramic

Transition $^4F_{3/2} \rightarrow {}^4I_{9/2}$	l (nm)	869	876	879	885	886	892	901	938	946
Nano Crystal β(0.341) τ_{rad} (0.275 ms)	Δn (cm^{-1})	16.9	15.5	30.1	21.5	25.5	24.9	36.2	17.5	15.7
	$A_{ij}(S^{-1})$	81.7	40.4	63.8	223.2	345	275	271	297	441
	$\sigma_e(10^{-20}\ cm^2)$	1.56	0.85	0.7	3.47	4.54	3.75	2.59	6.37	10.7
Single Crystal β(0.370) τ_{rad} (0.250 ms)	Δn (cm^{-1})	17.3	13.5	25.7	24.7	25.3	25.4	39.0	17.8	16.7
	$A_{ij}(S^{-1})$	104.4	49.0	76.7	295.8	378.1	323.7	323.8	347.8	532.7
	$\sigma_e(10^{-20}\ cm^2)$	1.73	1.06	0.87	3.54	4.44	3.84	2.55	6.52	10.8
Ceramic β(0.351) τ_{rad} (0.274 ms)	Δn (cm^{-1})	16.3	13.7	24.7	25.7	25.8	25.8	39.2	17.2	16.8
	$A_{ij}(S^{-1})$	90.4	42.4	66.5	256.1	327.3	280.1	280.2	301.1	461.1
	σ_e ($10^{-20}\ cm^2$)	1.50	0.91	0.76	3.1	3.8	3.3	2.2	5.65	9.32

Table 4. Radiative Properties of Various Stark Levels Observed for the Transition within the Manifold $^4F_{3/2} \rightarrow {}^4I_{11/2}$, and Its Comparison with the Single Crystal and Ceramic

Transition $^4F_{3/2} \rightarrow {}^4I_{11/2}$	l (nm)	1052	1055	1062	1064	1068	1075	1079	1106	1112	1116	1123
Nano Crystal β(0.536) τ_{rad} (0.275 ms)	Δn (cm^{-1})	9.85	16.7	9.2	10.2	20.2	10.3	15.4	24.4	16.5	20.9	16.8
	$A_{ij}(S^{-1})$	211	24	518	895	277	348	259	193	232	149	149
	$\sigma_e(10^{-20}\ cm^2)$	10.1	0.66	27.3	42.7	6.6	16.7	8.35	4.15	7.46	3.78	4.78
Single Crystal β(0.500) τ_{rad} (0.250 ms)	Δn (cm^{-1})	7.7	20.3	9.1	10.6	16.6	10.6	15.2	20.6	16.6	20.7	16.7
	$A_{ij}(S^{-1})$	135	18	538	949	256	364	261	195	234	151	151
	$\sigma_e(10^{-20}\ cm^2)$	7.35	0.45	25.2	38.5	6.68	15.1	7.6	4.39	6.63	3.46	4.33
Ceramic β(0.528) τ_{rad} (0.274 ms)	Δn (cm^{-1})	5.88	18.9	11.34	11.9	11.6	4.5	8.7	15.4	13.6	13.88	10.9
	$A_{ij}(S^{-1})$	246	11	478	993	202	342	242	207	208	157	157
	$\sigma_e(10^{-20}\ cm^2)$	17.5	0.42	18.9	37.6	7.5	33.2	12.2	6.25	7.21	5.36	6.93

#159671 - $15.00 USD Received 15 Dec 2011; revised 3 Feb 2012; accepted 6 Feb 2012; published 8 Feb 2012

Table 5. Radiative Properties of Various Stark Levels Observed for the Transition within the Manifold $^4F_{3/2} \rightarrow {}^4I_{13/2}$, and Its Comparison with the Single Crystal and Ceramic

Transition $^4F_{3/2} \rightarrow {}^4I_{13/2}$	l (nm)	1320	1335	1336	1339	1341	1354	1357	1358	1414	1431	1444
Nano Crystal β(0.117) τ_{rad} (0.275 ms)	Δn (cm^{-1})	12.4	11.1	10.2	10	11.7	11.2	6.0	6.9	13.4	14.5	13.5
	$A_{ij}(S^{-1})$	167	92	110	145	85	37	45	49	37	29	34
	$\sigma_e(10^{-20}\ cm^2)$	10.1	6.38	8.27	11.2	5.6	2.5	5.87	5.58	2.34	1.74	2.24
Single Crystal β(0.126) τ_{rad} (0.250 ms)	Δn (cm^{-1})	12.3	8.82	8.83	8.46	13.4	9.54	6.50	6.50	14.1	14.2	12.9
	$A_{ij}(S^{-1})$	180	78	95	136	103	30	48.1	49.7	42.9	31.3	35.0
	$\sigma_e(10^{-20}\ cm^2)$	9.68	6.1	7.3	11.1	5.24	2.20	5.20	5.39	2.31	1.73	2.16
Ceramic β(0.115) τ_{rad} (0.274 ms)	Δn (cm^{-1})	12.4	8.9	9.2	9.4	13.6	10.2	6.7	6.7	15.1	15.1	13.1
	$A_{ij}(S^{-1})$	150	65.1	79.0	114	85.2	25.1	40.1	41.5	35.7	26.0	29.1
	$\sigma_e(10^{-20}\ cm^2)$	8.1	5.1	6.1	9.1	4.36	1.83	4.33	4.48	1.93	1.44	1.79

Table 6. Radiative Properties of Various Stark Levels Observed for the Transition within the Manifold $^4F_{3/2} \rightarrow {}^4I_{15/2}$, and Its Comparison with the Single Crystal and Ceramic

Transition $^4F_{3/2} \rightarrow {}^4I_{15/2}$	l (nm)	1739	1752	1759	1769	1773	1784	1801	1877	1893
Nano Crystal β(0.006) τ_{rad} (0.275 ms)	Δn (cm^{-1})	13.84	5.97	5.98	13.7	15.76	12.9	18.5	9.1	7.95
	$A_{ij}(S^{-1})$	3.24	0.82	0.83	4.01	5.05	4.74	4.36	3.86	6.77
	$\sigma_e(10^{-20}\ cm^2)$	0.31	0.18	0.18	0.39	0.44	0.50	0.28	0.53	0.13
Single Crystal β(0.004) τ_{rad} (0.250 ms)	Δn (cm^{-1})	10.58	10.9	9.20	10.5	11.86	11.24	17.63	1156	8.60
	$A_{ij}(S^{-1})$	1.99	0.58	0.77	3.16	4.63	3.13	3.18	3.89	4.92
	$\sigma_e(10^{-20}\ cm^2)$	0.22	0.64	0.11	0.36	0.47	0.34	0.22	0.46	0.79
Ceramic β(0.0.006) τ_{rad} (0.274 ms)	Δn (cm^{-1})	11.52	11.84	9.10	11.49	11.78	11.52	18.63	12.6	8.7
	$A_{ij}(S^{-1})$	2.73	0.80	1.05	4.32	6.34	4.28	4.36	5.32	6.74
	$\sigma_e(10^{-20}\ cm^2)$	0.30	0.09	0.14	0.49	0.65	0.46	0.29	0.63	1.08

$$\sigma(J, J'; \tilde{\nu}) = \frac{\lambda^2}{8\pi c n^2} \frac{\beta(J, J')}{\tau_J} g(\tilde{\nu}), \tag{4}$$

where λ is the wavelength at the peak emission, $\tilde{\nu} = \lambda^{-1}$ is the wave number, β (J, J') is the fluorescence branching ratio for the transition from the upper manifold J to the lower manifold J', τ_J is the radiative lifetime of the excited manifold J (J = 3/2), and $g(.)$ is the line shape function. The line shape function was obtained from the fluorescence spectrum using the following expression [28]

$$g(\tilde{\nu}) = \frac{I(\tilde{\nu})}{\int I(\tilde{\nu}) d\tilde{\nu}}, \tag{5}$$

where $I(\tilde{\nu})$ is the intensity at $\tilde{\nu}$. The line shape functions for the transitions within the manifold $^4F_{3/2} \rightarrow {}^4I_{9/2}$, $^4F_{3/2} \rightarrow {}^4I_{11/2}$, $^4F_{3/2} \rightarrow {}^4I_{13/2}$, and $^4F_{3/2} \rightarrow {}^4I_{15/2}$ can therefore be determined by dividing the peak intensities $I(\tilde{\nu})$ by the integrated areas of the respective fluorescence spectra. The values of $g(\tilde{\nu})$, along with the values of radiative lifetime and intermanifold branching ratios from Table 2, and the values of λ and n are applied to Eq. (4) to determine the emission cross sections for the $^4F_{3/2} \rightarrow {}^4I_{9/2}$ and $^4F_{3/2} \rightarrow {}^4I_{11/2}$, $^4F_{3/2} \rightarrow {}^4I_{13/2}$ and $^4F_{3/2} \rightarrow {}^4I_{15/2}$ intermanifold transitions. The emission cross-sections calculated for the

#159671 - $15.00 USD Received 15 Dec 2011; revised 3 Feb 2012; accepted 6 Feb 2012; published 8 Feb 2012

transitions within the manifolds ${}^4F_{3/2} \rightarrow {}^4I_{9/2}$ and ${}^4F_{3/2} \rightarrow {}^4I_{11/2}$, ${}^4F_{3/2} \rightarrow {}^4I_{13/2}$ and ${}^4F_{3/2} \rightarrow {}^4I_{15/2}$ of Nd: YAG nanocrystals are reported in Table 7. These values for the Nd: YAG nanocrystals are found to be very much similar to single crystal and ceramic with some experimental uncertainties.

Table 7. Spectroscopic Properties of 1.5% Nd^{3+} Doped YAG Nano Particles and Its Comparison with 1% Nd^{3+} Doped YAG Single Crystal and Ceramic

Parameters	Nano Crystal	Single Crystal	Ceramic
Ω_2 x 10^{-20} cm^2	0.22	0.22	0.2
Ω_4 x 10^{-20} cm^2	3.15	3.55	4.69
Ω_6 x 10^{-20} cm^2	5.71	5.33	5.00
τ_{rad} (${}^4F_{3/2} \rightarrow {}^4I_{9/2}$) μs	275	238	250
σ_e (${}^4F_{3/2} \rightarrow {}^4I_{9/2}$) cm^2	3.91 x 10^{-19}	4.65 x 10^{-19}	4.01 x 10^{-19}
σ_e (${}^4F_{3/2} \rightarrow {}^4I_{11/2}$) cm^2	7.80 x 10^{-19}	7.31 x 10^{-19}	7.23 x 10^{-19}
σ_e (${}^4F_{3/2} \rightarrow {}^4I_{13/2}$) cm^2	5.74 x 10^{-19}	5.88 x 10^{-19}	6.19 x 10^{-19}
σ_e (${}^4F_{3/2} \rightarrow {}^4I_{15/2}$) cm^2	0.36 x 10^{-19}	0.19 x 10^{-19}	0.35 x 10^{-19}
β (${}^4F_{3/2} \rightarrow {}^4I_{9/2}$) %	34.1	40.9	37.0
β (${}^4F_{3/2} \rightarrow {}^4I_{11/2}$) %	53.6	48.1	50.0
β (${}^4F_{3/2} \rightarrow {}^4I_{13/2}$) %	11.7	10.8	12.6
β (${}^4F_{3/2} \rightarrow {}^4I_{15/2}$) %	0.6	0.2	0.4

3.3 Scattering loss

The scattering loss coefficients of Nd^{3+}: YAG and pure YAG nanocrystals were calculated using Fresnel's equation and compared with those of single crystals and ceramics. Since the dopant concentration of Nd^{3+} is low, the refractive indexes used were taken from the literature for YAG nanocrystals [31]. The scattering loss coefficient, α (λ), was determined using the following equation [2,6,28];

$$\alpha(\lambda) = -t^{-1} \ln\left[I(\lambda) / I_0(\lambda) T(\lambda)^2 \right], \tag{6}$$

where $I(\lambda), I_0(\lambda), T(\lambda),$ and t denote the transmission light intensity of the sample at a particular wavelength λ, incident light intensity, Fresnel loss correction factor, and the sample thickness. The value of $I(\lambda) / I_0(\lambda)$ was estimated from the background level of the transmittance because of the Nd^{3+} absorption. The Fresnel surface loss, $\beta(\lambda)$ assuming normal incidence and absorption was calculated using the following expression;

$$\beta(\lambda) = \left[(n(\lambda) - 1)^2 / (n(\lambda) + 1)^2 \right], \tag{7}$$

where $n(\lambda)$ is the refractive index at wavelength λ. The correction factor is obtained by, $T(\lambda) = 1 - \beta(\lambda)$. Since the calculation is based on the transmission spectrum along with its background level of transmittance and compared with the absorption spectra, all the scattering centers are included into the calculation. Based on the wavelength of light used, size of particles and their agglomeration size, and difference in relative refractive index between epoxy (1.556) and the particles (1.7-1.85), one can easily conclude that scattering [32] is one of the dominating loss within these nanocrystals mixed with the epoxy. Since the agglomeration size of the YAG nanocrystals (400 to 500 nm) approaching the optical wavelength used as shown in Fig. 2(c), the scattering loss in nanocrystals have been found more in UV range as shown in Fig. 7. The calculation shows that maximum scattering loss is 3.42 cm^{-1} at 400 nm, where the scattering loss is 1.43 cm^{-1} at the excitation wavelength (800 nm). Furthermore, the scattering intensity was estimated using Rayleigh's equation [6] and the ratio of 400 nm to 800 nm scattering loss intensity was calculated to be 14:1. This verifies that wavelength dependent scattering loss in nanocrystals is significantly high compared to those of ceramics and single crystals. The scattering loss in ceramics is due to the existence of

#159671 - $15.00 USD Received 15 Dec 2011; revised 3 Feb 2012; accepted 6 Feb 2012; published 8 Feb 2012

the grain boundary but the calculation shows that single crystals also has some scattering centers which are unknown and needs more analysis.

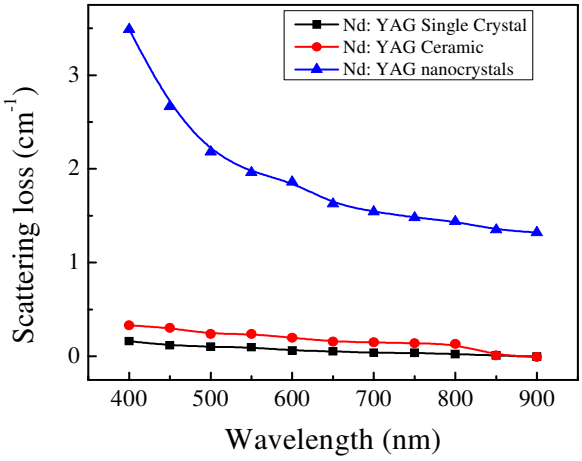

Fig. 7. Dependance of scattering loss coefficients of Nd^{3+}: YAG nanocrystals to wavelength and its comparison with single crystal and ceramic.

3.4 Non-radiative processes and internal quantum yield

A quantitative way of measuring the internal quantum yield for a particular emission band is done through the fluorescence lifetime measurements. Non-radiative processes such as multi-phonon relaxation, vibrational losses by surface (such as hydroxyl) species and energy transfer (ET) interactions quench the fluorescence intensity and the efficiency. The observed lifetime of the emission can be written as [33].

$$\frac{1}{\tau_{lum}} = A_{rad} + W_{mp} + W_{OH} + W_{ET}, \tag{8}$$

where A_{rad}, W_{mp}, W_{OH}, W_{ET} are the radiative transition rate, transition rate from multiphonon relaxation, hydroxyl groups and energy transfer interaction respectively. The contribution to non-radiative decay comes from multi-phonon relaxation from the host and energy transfer interactions between nearby ions. The transition probability by energy transfer is dependent on the distance between the donor (D) and acceptor (A) ions, R_{DA}, and hence dependent on the concentration of the ions. When the ions are homogeneously distributed in the matrix, the energy transfer relaxation rate W_{ET} can be written as [34].

$$W_{ET} \alpha \frac{1}{R_{DA}^6} \alpha N^2, \tag{9}$$

where N is the dopant concentration. Since the dopant concentration in this sample is (1.5 at %) low, ET has nominal contribution for lowering the fluorescence lifetime and intensity. On the other hand, the radiative transition probabilities and multi-phonon relaxation rates do not depend on the dopant concentration. The values of W_{OH} and W_{mp} can be determined from quantitative measurements of the OH content and from the low frequency vibrational modes in the sample measured from the infrared FTIR spectrum shown in Fig. 8. Multiphoton non-radiative loss (W_{mp}) was calculated using the following equation [35]

$$W_{mp} = B \exp^{-\alpha \Delta E}, \tag{10}$$

#159671 - $15.00 USD Received 15 Dec 2011; revised 3 Feb 2012; accepted 6 Feb 2012; published 8 Feb 2012

where ΔE is the energy gap between the manifold transition $^4F_{3/2} \rightarrow {}^4I_{11/2}$, the other parameters B and α are constant taken from literature [35]. Using these values, the multi-phonon vibrational loss for the 1060 nm emission band was calculated to be 0.000001cm^{-1}, which is negligible. Thus the major contribution for the non-radiative decay is coming from the water present in the sample which is confirmed by the absorption band at 3450 cm^{-1} in the FTIR spectrum shown in Fig. 8. The amount of water content in the samples can be obtained from the measurement of the absorption coefficient at the OH peak of the IR spectrum and is estimated to be nearly 19.5 cm^{-1}. An OH concentration of 360 ± 100 ppm gives absorption of ~2.8 cm^{-1} [36]. By comparison, the corresponding water content was estimated to be 2507 ppm (4.0 x 10^{20} molecules/cm^3). The major sources of OH content in the Nd^{3+}: YAG nanocrystals are from the starting chemicals and atmosphere during synthesis. A higher level of water content can be suppressed by using moisture free chemicals melted in water free environment

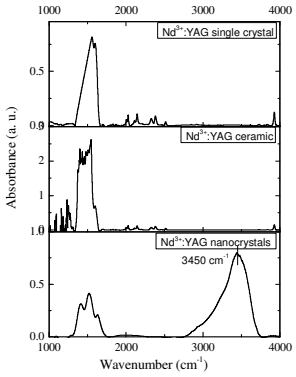

Fig. 8. FTIR spectrum of Nd^{3+}: YAG nanocrystals compared to single crystal and ceramics.

The internal quantum efficiency, (η_{Int}) can be evaluated from the ratio of the fluorescence lifetime to radiative decay time [25,32]. The fluorescence decay time obtained for the Nd^{3+}: YAG nanocrystals corresponding to 1060 nm is 70 μs as shown in Fig. 9, which is significantly low compared to >230 μs for single crystal and ceramics. This gives an internal quantum yield of 25.4% for the transition through $^4F_{3/2}$ which is significantly less compared to > 75% for ceramic and single crystal. This shows that the major non-radiative losses are coming from the surface hydroxyl groups for present nanoparticles, which is absent in the single crystal and transparent ceramic as evidenced from the FTIR spectra in Fig. 8.

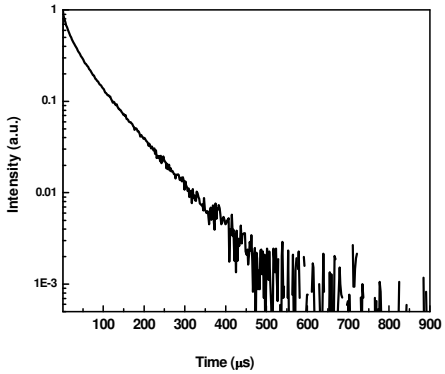

Fig. 9. Fluorescence decay curve for 1060 nm emission in Nd^{3+}: YAG nanocrystals.

#159671 - $15.00 USD Received 15 Dec 2011; revised 3 Feb 2012; accepted 6 Feb 2012; published 8 Feb 2012

4. Conclusions

Comparison of the radiative and non radiative spectral properties such as absorption cross sections, fluorescence branching ratios, emission cross sections of the inter-Stark transitions and cross sections of the intermanifold transitions show that most of the radiative spectral properties of the three hosts are in good agreement. However the fluorescence decay time and hence the quantum efficiency of the nanocrystal was too low due to the presence of large quantity of hydroxyl groups on the nanoparticle surface. In addition, because of the large agglomeration of the particles with average size of around 400 nm, wavelength dependent optical loss calculated using Fresnel's equation for the Nd^{3+} doped YAG nanocrystals is significantly high compared to those of Nd^{3+} doped single crystals and ceramics. Thus in practical applications of this nanocrystals for making transparent ceramics for laser or other photonics application, careful heat treatment and water free synthesis has to be adopted to achieve high fluorescence quantum yield.

Acknowledgments

This research was sponsored by the National Science Foundation (NSF) Partnerships for Research and Education in Materials (PREM), Grant Number: DMR-0934218. The authors would like to thank Dr Uwe Hommerich at Hampton University, experimental assistance in lifetime measurements on Nd^{3+}: YAG nanocrystals.

#159671 - $15.00 USD Received 15 Dec 2011; revised 3 Feb 2012; accepted 6 Feb 2012; published 8 Feb 2012